LABORATORI NAZIONALI DI FRASCATI
SIS-Pubblicazioni

Commissioning of the DAΦNE Beam Test Facility

G. Mazzitelli and P. Valente
Laboratori Nazionali di Frascati dell'INFN, Frascati, Italy.

Abstract

The DAΦNE Beam Test Facility (BTF) is a beam transfer line optimized for the production of a defined number of electrons or positrons, in a wide range of multiplicities and down to single-electron mode, in the energy range between 50 and 800 MeV. The typical pulse duration is 10 ns and the maximum repetition rate is 50 Hz. The facility is aimed mainly for detector calibration purposes. The BTF has been successfully commissioned in February 2002, and started operation in November of the same year. The schemes of operation, the commissioning results, as well as the first users' experience are here reported.

Contents

1 Introduction

The Beam Test Facility (BTF, see logo in Fig. 1) is part of the DAΦNE ϕ-factory complex [1], which includes a high current electron and positron LINAC, a spectrometer line, a 510 MeV e$^-$ and e$^+$ accumulator, and two 510 MeV storage rings (with transfer lines from the LINAC and accumulator). The e$^+$/e$^-$ beam produced by the LINAC is stacked and damped in the accumulator ring, from which it is extracted and injected in the main rings. When the injector system is

Figure 1: The BTF logo.

not delivering beams to the accumulator, the LINAC beam, suitably attenuated, can be trasported into the beam test area by a transfer line (BTF line). The DAΦNE complex layout and its main components are shown in Fig. 2.

The BTF facility has been designed [2] to provide a defined number of particles in a wide range of multiplicities and energies, mainly for detector calibration purposes. In the following, after a brief description of the transfer line layout, the scheme for single particle production is discussed; the energy selection system and its resolution are described; then the detectors used for the beam diagnostics and some measurements of beam characteristics during the commissioning phase are described. Finally, a "parasitic" and "dedicated" use of the BTF is briefly discussed together with the operational experience during the first users access to the facility.
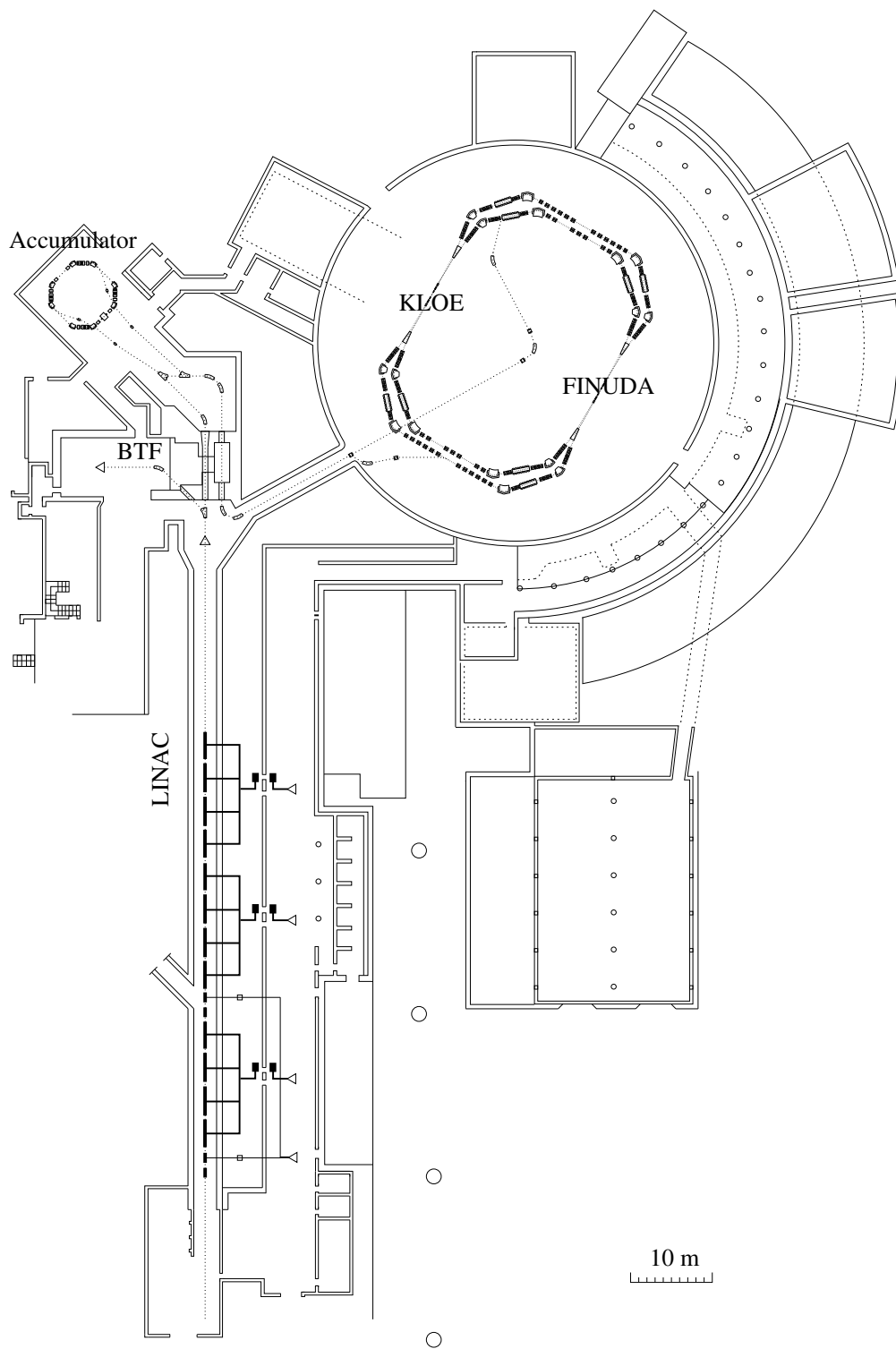
Figure 2: Plan of the DAΦNE complex, showing the LINAC, the accumulator, the main rings and the beam test facility (BTF).

4

2 BTF description

2.1 BTF line

The part of the transfer line relevant for the BTF – from the LINAC to the test area and the beam line exits – together with their main elements, are shown in Fig. 3; the main elements of the injector system and of the BTF line are:

- the DAΦNE **LINAC**: it delivers electrons with energy up to 800 MeV, with a maximum current of 500 mA/pulse, or positrons with energy up to 550 MeV, with a maximum current of 100 mA/pulse; the typical pulse duration is 10 ns with a maximum repetition rate of 50 Hz. When injecting for the operation of the main rings at the ϕ resonance, the beam energy is 510 MeV. The main LINAC parameters are summarized in Tab. 1.

- the **transfer line**: just after the LINAC, it drives particles to the DAΦNE accumulator ring, and from there to the main rings. A 45° bending magnet (`DHSTB01` in Fig. 3) allows to alternatively send the beam to the BTF area.

- the **spectrometer line**: at the beginning of the transfer line a pulsed 6° dipole magnet can deliver some of the pulses from the LINAC to a separate line, usually at one pulse per second (1 out of 50 at the maximum injection repetition rate), where the beam energy is measured by means of a 60° bending magnet (`DHSTS01` in Fig. 3) coupled to a metallic strips segmented detector (hodoscope), with a typical accuracy of $\approx 0.2\%$ [5].

- a selectable **target**: almost half-way of the DAΦNE transfer line, a tungsten target (`TGTTM01` in Fig. 3) allows to strongly attenuate the LINAC beam for the BTF purposes. The target is shaped in such a way that three different radiation lengths can be selected (see Sec. 3.2) by inserting it at different depths into the beam-pipe.

- an **energy selector**: the 45° bending magnet after the target mentioned above (`DHSTB01` in Fig. 3), has a double task: it deviates the attenuated beam to the BTF hall and, together with a downstream collimator, selects the momentum of the particles.

- the **final bending** magnet: the energy selector is followed by a ≈ 12 m transfer line, up to the BTF experimental hall where the experimental set-ups can be installed. A the end of this line a second bending magnet (`DHSTB02` in Fig. 3) allows to use two separate test lines: one directly from the straight section (dipole off), one coming out from the magnet at 45° (dipole on).
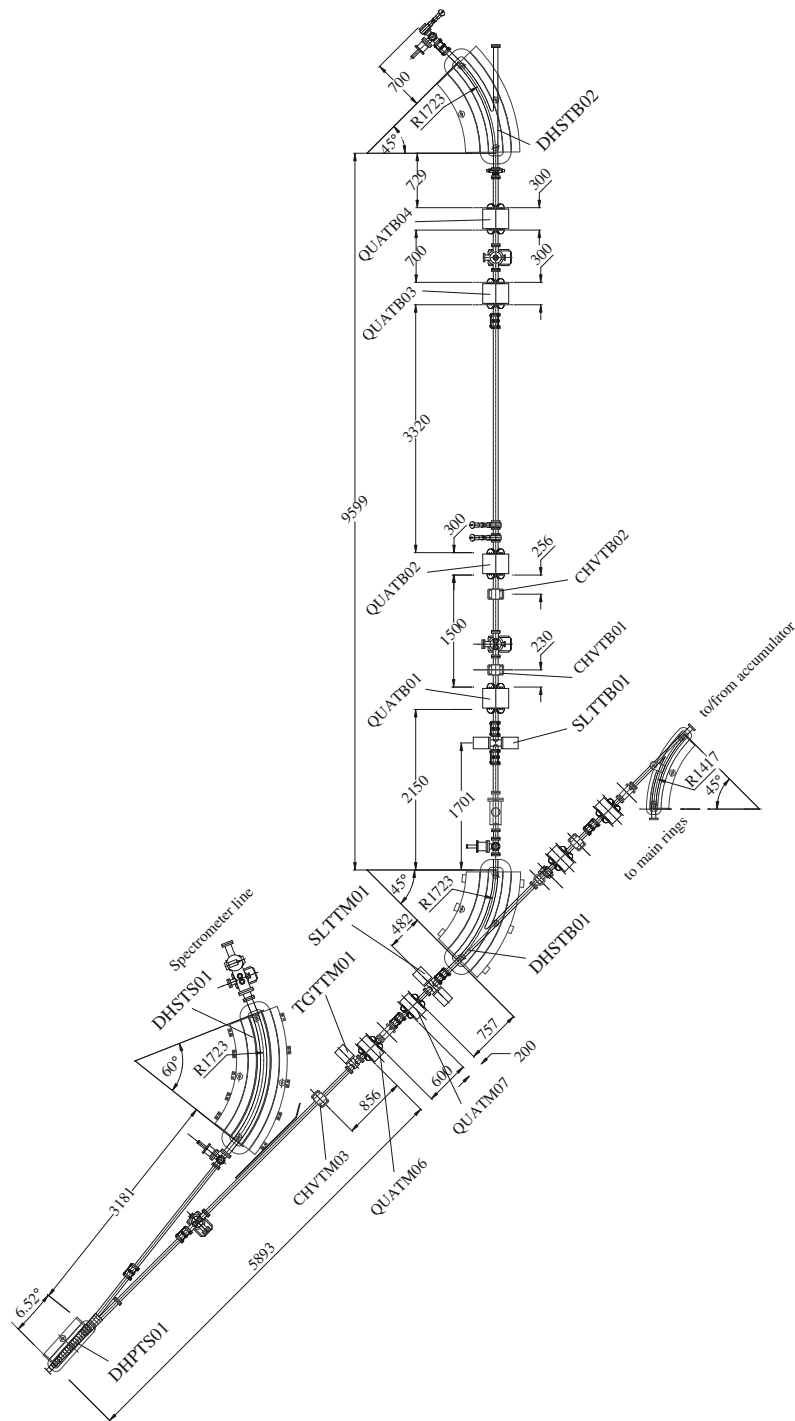
5

Figure 3: Plan of the transfer line from the LINAC exit to the BTF hall, showing all the relevant elements: the pulsed magnet (DHPTS01) sending one pulse out of 50 (25) to the LINAC spectrometer (dipole DHPTS01 and metallic strips detector), the target (TGTTM01), the slits before (SLTTM01) and after (SLTTB01) the first bending magnet (DHSTB01), and finally the second bending at the end of the BTF transfer line (DHSTB02).

Parameter	Value
Energy range	$50 \div 800$ MeV (e^-) $50 \div 550$ MeV (e^+)
Transverse emittance at 510 MeV	1 mm mrad (e^-) 5 mm mrad (e^+)
Energy spread at 510 MeV	1% (e^-) 2% (e^+)
Repetition Rate	$0 \div 50$ Hz
Pulse Duration	10 ns (RF 2.865 GHz)
Maximum current	500 mA/pulse (e^-) 100 mA/pulse (e^+)

Table 1: The main parameters of the DAΦNE LINAC.

All magnetic elements (dipoles, correctors and quadrupoles), as well as the slits and degrader target, are remotely controlled and fully integrated in the DAΦNE control system [3,4].

2.2 BTF hall and equipment

The experimental area (once used as "Pion Test Facility" during the operation of the ADONE accelerator) is extended over a 100 m^2 area, it has two independent entrance doors, a 6 m high ceiling, it is surrounded by shielding walls of (movable) concrete blocks, and a 20 ton crane is available.

The plan of the experimental hall, showing the two transfer line outputs and the position of the concrete shielding blocks, is shown in Fig. 4, while in Fig. 5 a photograph shows part of the transfer line (in the LINAC tunnel). Nearby to the experimental area a (dedicated) control room allows to conveniently run the facility and the users set-ups through a number of coaxial cables stretched between the hall and the control room.

The facility is equipped with a number of devices and crates, for controlling the magnets and the other elements of the line, integrated in the accelerator controls. In addition, a VME crate is dedicated to the acquisition of the BTF diagnostics, consisting essentially of particle detectors (described with some details in the following, Sec. 4.1 and Sec. 4.4). Some equipment is also available for the users needs, including scintillator pallets, HV crates, a VME crate with CAMAC branch and VME controller CPU.

Door

Control Room

h3 h3 h3 h3 h3 h3

h3

h3 h3

h3 h3

h3

h3 h3

h3

X

X h3 h3 h3 h3 h3 h3 h3

h3 h3

h3

h3 h3

h3 h3 h3

h3 h3 h3

Door h3

h3 h3

h3 h3

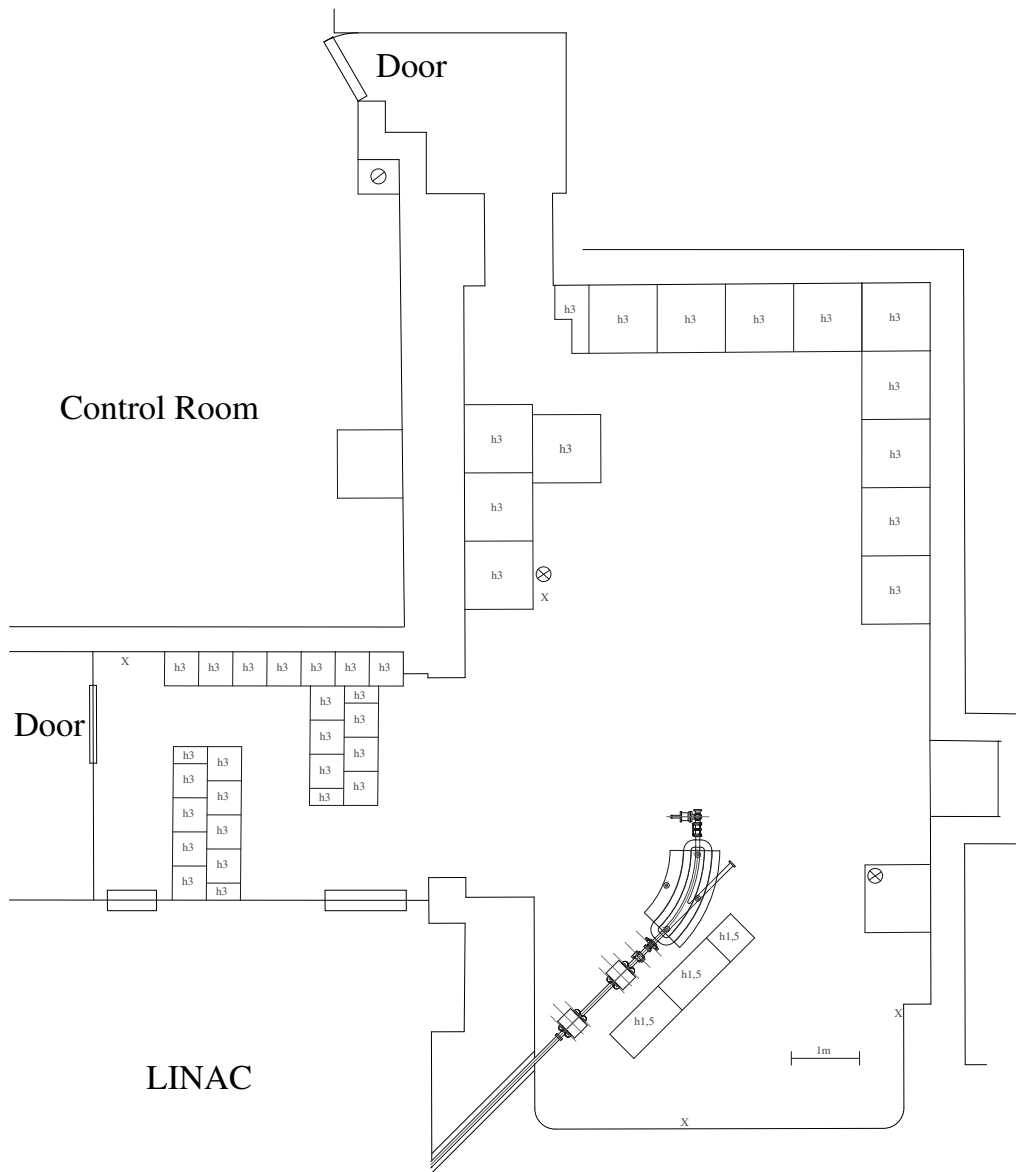h3 h3

h3 h3

h3 h3

h1,5

h1,5

h1,5

X

1m

LINAC

X

Figure 4: Plan of the BTF experimental hall, showing the final part of the transfer line with the second bending magnet (DHSTB02). The concrete blocks of the shielding walls are also shown.

Figure 5: Photograph of the transfer line to the BTF (in the LINAC tunnel). On the left, from the foreground: the bending magnet of the selector (DHSTB01), followed by a "flag" (FL1TB01), the slits (SLTTB01) and a quadrupole (QUATB01); on the right, in the background, the transfer line of the accumulator ring (DHPT02).

The BTF is also equipped with a complete gas system in order to allow the operation of gas detectors. Four independent stainless steel lines connect a gas-packs area, located just outside the hall, with the experimental area, providing four pressure-reduced heads dedicated to different kind of gases: carbon dioxide, isobutan, ethane and argon (or noble gases).

Finally, a remotely controlled, motorized trolley (2×1 m^2 area) is also available for moving detectors.

3 Main parameters and operation mode

The minimum LINAC beam current that can be conveniently measured by the DAΦNE current monitors is $I \approx 1$ mA. Being the typical pulse duration $t = 10$ ns (this value is optimized for the injection in the main rings, and could not be changed during 2002 runs, see Sec. 5.1), this corresponds to a number of particles:

$$N = \frac{I t}{e} = 6.24 \times 10^7.$$

It is thus necessary to strongly reduce the number of primary e^- (e^+) delivered by the LINAC to reach the few particles range.

The reduction of the particle multiplicity can be achieved with different methods, the one chosen for the BTF operation is the following: first the LINAC beam is intercepted by a (variable depth) target in order to "degrade" the beam energy, then the outcoming particles are energy selected by means of a bending magnet and slit system. The degrader target, indeed, highly increases the energy spread of the primary beam; on the other hand the energy selector only accepts a small fraction of the resulting energy distribution, thus giving a reduction of the number of electrons by a large and tunable factor.

This beam attenuation system is schematized in Fig. 6; the main parameters which determine the particle number reduction are the target depth and the energy acceptance of the selector, and are briefly discussed in the following (a more detailed description can be found in Ref. [2]).
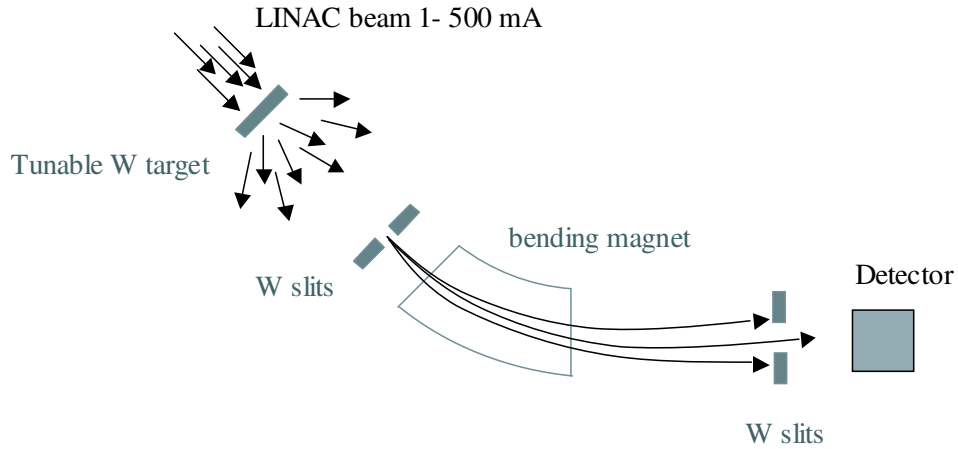

Figure 6: Beam attenuation and energy selection scheme.

The tungsten degrader target (`TGTTM01`, see Fig. 3) is shaped in such a way that three radiation lengths, $1.7, 2.0, 2.3\ X_0$, can be selected by inserting it at different depths into

the beam-pipe, as schematically shown in Fig. 7: the (transverse) width between the three different positions (1,2,3 in Fig. 7) is 50 mm, while the distance from the beam-pipe center of the target profile (position 0), when it is totally extracted, is 31 mm.
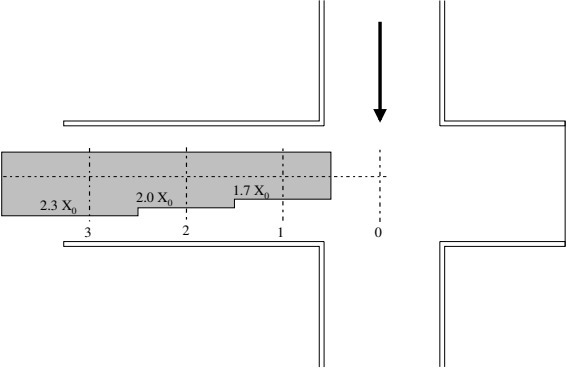

Figure 7: Schematic view of the tungsten target `TGTTM01`.

3.1 Energy selection resolution

In order to evaluate the energy selection resolution, *i.e.* the energy acceptance of the selector, the geometry of the system has to be taken into account. The definition of the relevant parameters, such as the slit apertures and distances, are shown in Fig. 8.
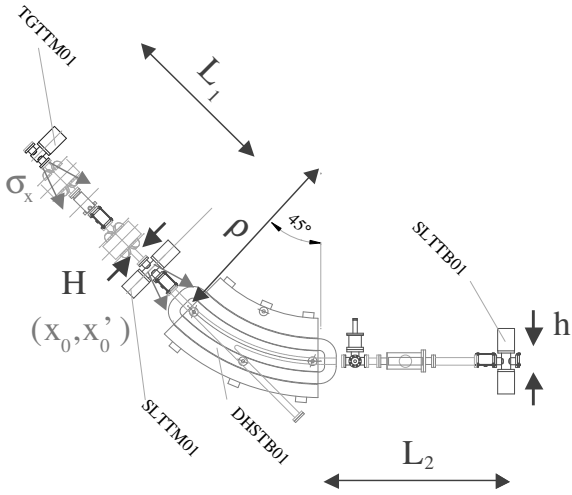

Figure 8: Definition of the quantities relevant for the energy selector resolution: magnetic radius of curvature of the dipole, slit apertures and distances.

Due to the momentum dispersion introduced by the bending magnet, the relative energy spread $\Delta E/E$ is proportional to the relative angular dispersion $\Delta \alpha/\alpha$, and is essentialy

11

determined by the magnet/collimator distance, L_2, by the dipole magnet radius of curvature, ρ, and by the slit aperture, h. A further contribution to $\Delta\alpha/\alpha$ comes from the beam divergence already present at the *entrance* of the bending magnet, x'_0.

Since $L_2 \simeq \rho$ ($\rho = 1723$ mm, $L_2 = 1701$ mm), the energy resolution can be written as:

$$\left|\frac{\Delta E}{E}\right| \simeq \frac{h}{2L_2} + \sqrt{2}\,|x'_0|_{\mathrm{max}} \tag{1}$$

In our case the beam divergence at the input of the bending magnet is limited by the presence of an upstream collimator (SLTTTM01). In addition, a non-negligible contribution to the divergence comes from the finite beam spot size *at the target*, σ_x, so that the divergence before the bending magnet is:

$$|x'_0|_{\mathrm{max}} \simeq \frac{\sigma_x + H/2}{L_1} \tag{2}$$

Combining Eq. (1) and Eq. (2), the total energy resolution is:

$$\left|\frac{\Delta E}{E}\right| = \frac{h}{2L_2} + \sqrt{2}\left(\frac{\sigma_x}{L_1} + \frac{H}{2L_1}\right) \tag{3}$$

The mechanical and positioning characteristics of the upstream and downstream slit systems are summarized in Tab. 2.

Inserting in Eq.(3) the typical values used in Nov.-Dec. 2002: $h = 5 \div 10$ mm, $H = 5 \div 10$ mm, $\sigma_x \simeq 5$ mm, a $\approx 1\%$ upper limit to the energy resolution can be estimated. Moreover, the σ_x/L_1 term is the most significant, so that $\Delta E/E$ does not depend much on the opening of the slits.

The nominal energy of the selector system, E_{sel}, is calculated from the current setting of the DHSTB01 magnet using its nominal magnetic length of 1.723 m and the experimental field/current excitation curve shown in Fig. 9: the relation is linear up to 400 A, corresponding to ≈ 590 MeV (the magnetic measurements were performed by the manufacturer, ANSALDO [6]).

An independent absolute calibration of the LINAC energy measurement performed by the DAΦNE spectrometer, is provided by the resonant production of the ϕ meson in the DAΦNE main rings with e^+e^- collisions, since the momentum acceptance of the accumulator ring is 1%.

3.2 Single electron production

To operate in the single particle mode, the incoming beam has to be attenuated by a factor as large as 10^8, by means of the degrader target and energy selection system discussed above. The most effective parameter that allows to adjust the number of particles in

Slit	Parameter	Value
Upstream (SLTTM01)	Transverse dimensions	30mm $\times$60 mm
	Depth	35 mm
	Aperture range	0.1 $\div$ 55 mm
	Positioning step	0.1 mm
Downstream (SLTTB01)	Transverse dimensions	35 mm $\times$70 mm
	Depth	35 mm
	Aperture range	0.1 $\div$ 62 mm
	Positioning step	0.02 mm

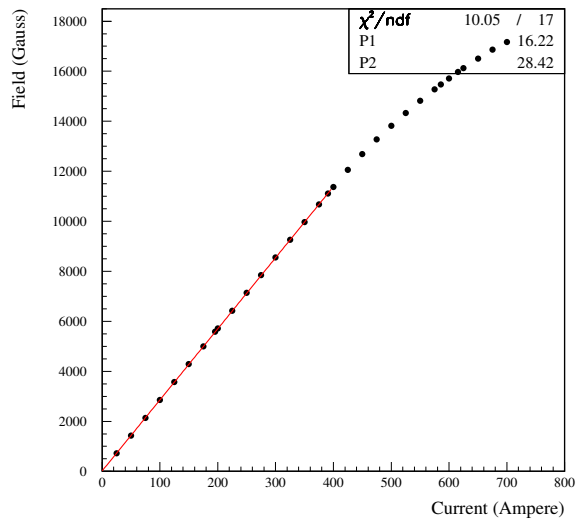Table 2: The main parameters of the energy selector (tungsten) slit system.

Figure 9: Excitation curve for `DHSTB01` magnet.

the beam is the selected energy, E_{sel}: by selecting different values of E_{sel} a different fraction of the degraded beam will be accepted. The expected multiplicity as a function of the selected energy can then be calculated by integrating the energy distribution of the particles emerging from the target over the accepted energy range ($\approx 1\%$ as shown before) around the chosen E_{sel} value.

A simple estimate of the energy distribution out of a target of depth $t = x/X_0$ in radiation lenghts can be obtained using the well-known formula, in the so-called "Rossi approximation B" [7], for an electromagnetic shower initiated by a particle of energy E_0:

$$f(E, E_0, t) = \frac{1}{E_0} \frac{[\ln(E/E_0)]^{\frac{t}{\ln 2} - 1}}{\Gamma\left(\frac{t}{\ln 2}\right)};$$ (4)

where Γ is the Euler function. The energy distribution calculated using Eq. (4) is shown in
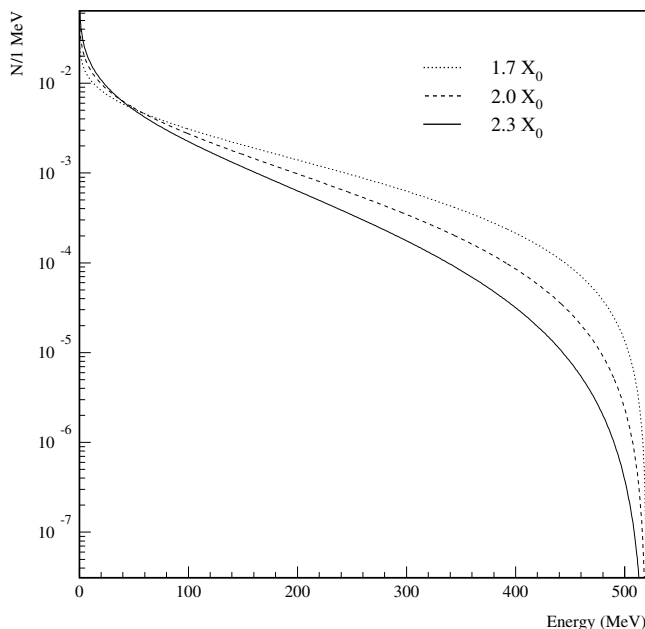

Figure 10: Electron energy distributions out of a 1.7,2.0,2.3 X_0 target, calculated according to the Rossi formula of Eq.(4).

Fig. 10. This distribution, however, does not take into account the angle of the emerging particles, because not all those secondary electrons will be accepted by the collimator and transported. Moreover, the beam-line itself limits the maximum angular divergence (in the vertical plane) to 6 cm/1.475 m ≈ 4 mrad.

In order to have a correct estimate of the expected number of particles as a function of the selected energy, a Monte Carlo simulation, based on GEANT [8], has been developed; the
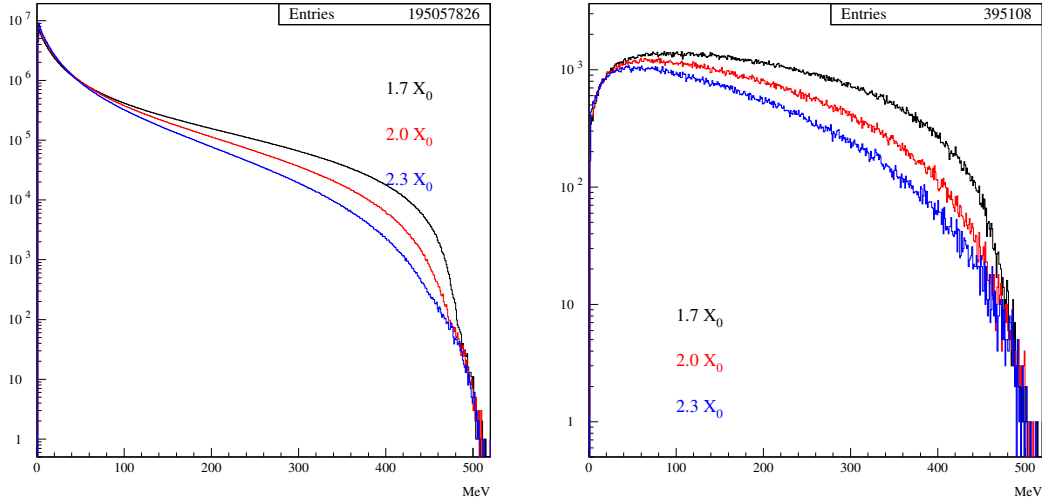
Figure 11: Electron energy distributions without (left) angular cut and for $\theta \leq 4$ mrad (right), for the three different degrader target depths, at the exit of the first slit collimator (`SLTTM01`), from the the Monte Carlo simulation of 10^8 primary electrons.

simulation takes into account the target and the upstream collimator, as well as the beam-pipe acceptance: the electron energy distributions without angular cut and for $\theta \leq 4$ mrad – corresponding to the beam-pipe acceptance (open collimator) – are shown, in Fig. 11 for the three possible target depths. A large number of Monte Carlo events have to be simulated to have a significant estimate also when very few particles survive, *i.e.* when E approches E_0. In the Monte Carlo distributions of Fig. 11, 10^8 primary electrons have been simulated, corresponding to a LINAC current of 1.6 mA (for a 10 ns pulse).

The number of accepted electrons as af function of E_{sel} is then simply calculated by integrating the energy distribution, with the proper angular cut for the chosen collimator aperture, around each E_{sel}. The integration range width should be chosen according to the energy resolution corresponding to each given collimator aperture. However, a 1% resolution is a good approximation for a wide range of slit apertures (as shown before): integrating the right distribution of Fig. 11 in 1% slices the expected number of electrons as a function of E_{sel} shown in Fig. 12 is finally obtained.

The number of particles estimated from the Monte Carlo simulation has to be considered as an upper limit, since it does not take into account the subsequent transport efficiency. Moreover, this simple estimate does not take into account the reduction due to the collimators. A detailed calculation of the transfer line efficiency would require to combine single-particle simulation codes (essentially based on `GEANT` [8]) with the beam transport calculation codes (such as `MAD` [9]), and is currently under study.
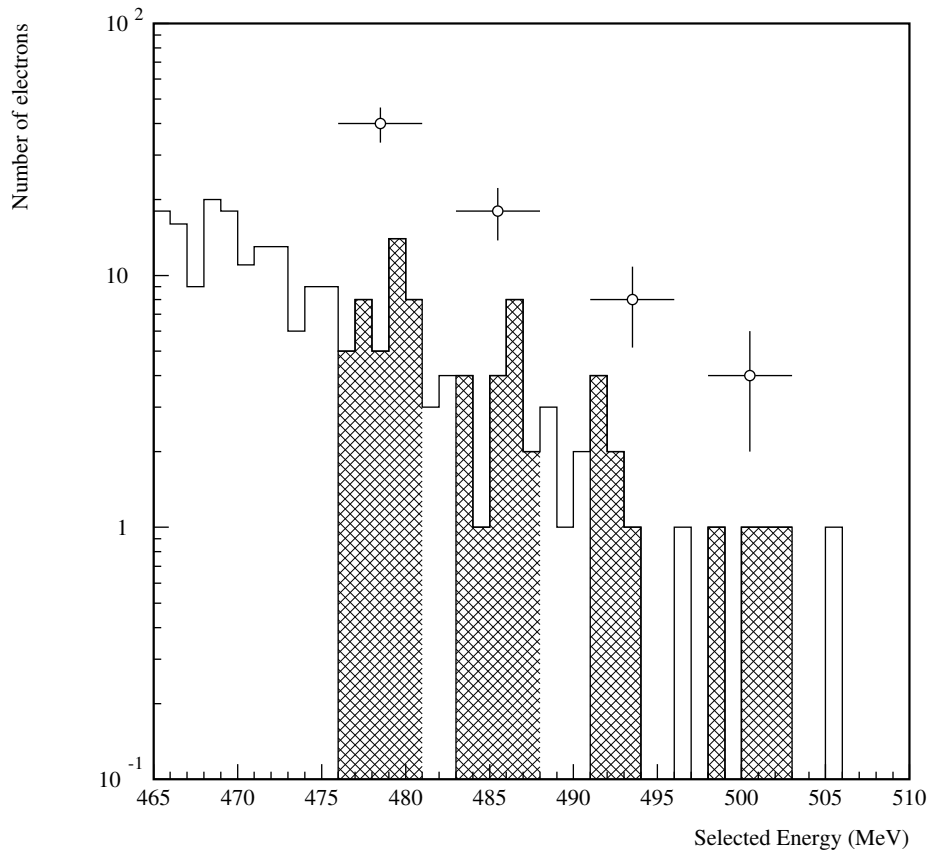
15

Figure 12: Integrating the energy distribution of electrons emerging from the target over 1% slices (shaded area), the expected number of particles as a function of the selected energy (open points) can be estimated from the Monte Carlo.

16

4   Commissioning results

The first phase of the BTF commissioning was carried on in February, 2002. In order to make a first optimization of the transport the beam position and size was monitored by means of a high-fluorescence target (flag FL1TB01). The very first beam injected in the BTF line – on Feb. 4, 2002 – is shown in Fig. 13 (the beam was dumped onto a lead Faraday cup).
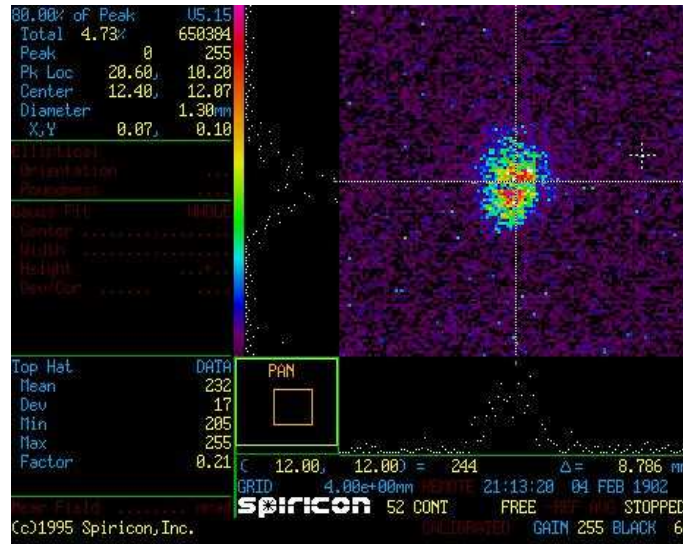

Figure 13: High-fluorescence target image of the first beam injected in the BTF hall, on Feb. 4, 2002.

In this phase we have also checked that the beam orbit was centered with respect to the beam-pipe; this was done by monitoring the (non-attenuated) beam with the fluorescent flag and with the LINAC beam position monitors, and by closing the collimators upstream and downstream the bending magnet (in a simmetric way). This is important in order to correctly set the energy out of the selector system. For radiation safety reasons, from then on no beam was allowed into the BTF hall without inserting the attenuating target.

At the beginning of the commissioning of the BTF line, a very low intensity electron beam was transported in the experimental hall: the minimum LINAC intensity attainable is ≈ 1 mA. This is dictated by the minimum intensity that can be effectively monitored by conventional beam diagnostic tools. No beam diagnostics at all is then available during BTF operation when the beam is attenuated by means of the target. In this case we could rely only on particle detectors.

17

4.1 Diagnostic detectors: calorimeters

Two different calorimeters have been used as main diagnostic devices, positioned at the two exits of the BTF line (as shown in the schemes of Fig. 14).
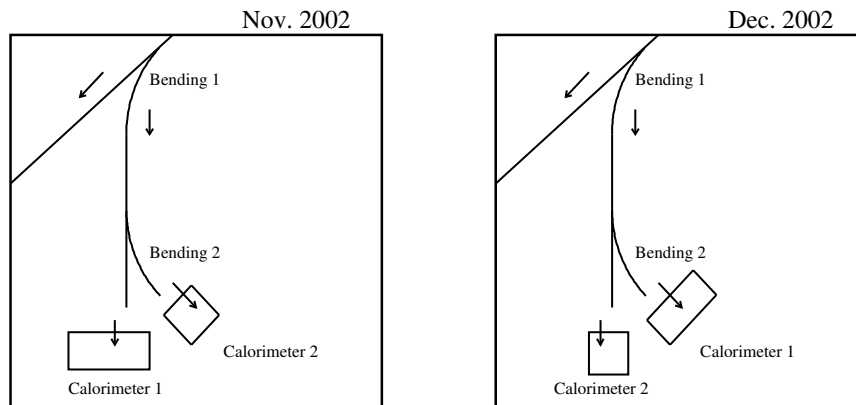

Figure 14: Positioning of the calorimeters during the Nov.-Dec. 2002 (right) commissioning.

Both detectors are lead/scintillating fibers calorimeters of the KLOE type [10], with single side photomultiplier readout. They are both composed by a stack of 0.5 mm thick grooved lead foils, alternating with an equal number of layers of 1 mm scintillating fibers (blue-green, type Po.Hi.Tech-0046), with 1.35 mm pitch, giving a 5 gr/cm^3 density composite. The two calorimeters have different readout segmentation:

Calorimeter 1: it is a cut-out of the KLOE barrel calorimeter *Prototype 0*, it is composed by ≈ 200 lead/scintillating fibers layers of 13.2×40 cm^2 for a total thickness of 24 cm, corresponding to $\approx 15X_0$. It is segmented in 4.4×4.4 cm^2 square cells with one-side only readout. For each cell the light is collected by a glued guide, consisting of a tapered mixing part with quadrangular entrance and circular exit terminating with a Winston cone, coupled to a Hamamatsu R1398 photomultiplier. A schematic view of the lead/fibers arrangement and of the segmentation of Calorimeter 1 is shown in Fig. 15; further details on this calorimeter can be found in Ref. [11].

Calorimeter 2: it is one of the small calorimeters used for the online measurement of the DAΦNE luminosity [12]. It has the same lead/fibers composition of Calorimeter 1, but has smaller transverse dimensions, 12.2×12.2 cm^2, and thickness, 18.4 cm, corresponding to $\approx 11.5X_0$. It is equipped with two plastic

18

guides concentrating the light onto a single 3" cathode photomultiplier (Hamamatsu H6155-01), as schematically shown in Fig. 15
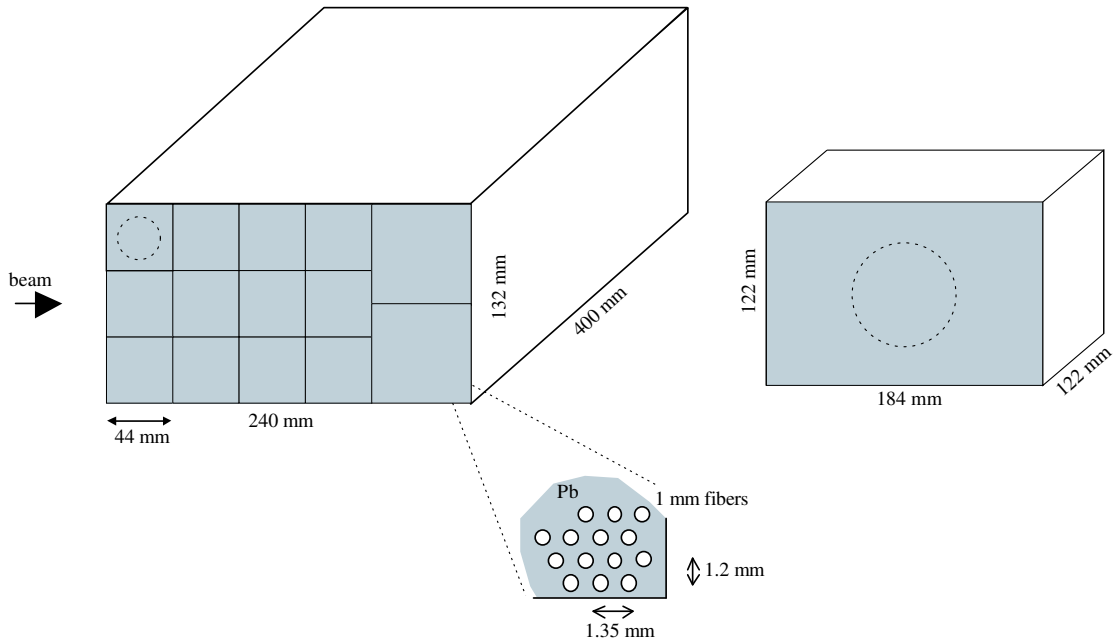

Figure 15: Schematic view of the calorimeters: "Calorimeter 1", the 14-cells KLOE calorimeter prototype 0 (left); "Calorimeter 2" the single-PMT DAΦNE luminometer (right).

The performances of this kind of calorimeter have been extensively studied [10,11]; the main features are a sampling fraction of $\approx 15\%$, a good energy resolution, and excellent timing resolution:

$$\sigma_E/E = 4.7\%/\sqrt{E(\text{GeV})}, \qquad \sigma_\text{t}/\text{t} = 54\text{ps}/\sqrt{E(\text{GeV})}.$$

The $14+1$ analog signals from the calorimeters are suitably delayed (≈ 200 ns) and are fed to a VME charge ADC (CAEN V792), with a resolution of 0.25 pC/count, integrating over a gate of 250 ns width. The gate signal is generated starting from a digital reference signal from the LINAC gun timing circuit (properly re-formed and timed). The analog signals are also digitized by means a VME low-threshold discriminator (CAEN V814) with a threshold of 35 mV/50Ω. The time of each channel is measured by means of a VME TDC (CAEN V775), in common stop mode (again given by the reference signal from the LINAC gun), with a resolution of 35 ps/count.
The VME controller is a VMIC 7740 Pentium III CPU with a Tundra VME-PCI bridge chip, running Red Hat Linux 7.2; the operating system is downloaded over a private Fast-

Ethernet network from a dedicated server (also running Red Hat Linux 7.2) that provides the remote filesystems for the data storage.

All the DAQ programs have been developed using the LabVIEW 6.0 environment with the following scheme: a low-level task continously runs on the VME controller CPU waiting for a new event; when a new event is found it reads the VME bus and stores all the read-out data in a temporary buffer of defined length (usually 100 events at 24+1 Hz repetition rate). A high-level task then accesses the data from the buffer and allows the user to store it to an output data file, to perform online-monitoring by means of histograms or time-charts. This run-control process (see Fig. 16) can be run on any of the DAΦNE control system machines in the DAΦNE private network. The relevant informations on the run conditions (date, number of events, magnet settings, slit settings, repetition rate, etc.) are also automatically stored into a relation database on a dedicated MySQL server, and are accessible as an "electronic logbook" from the BTF Web site.
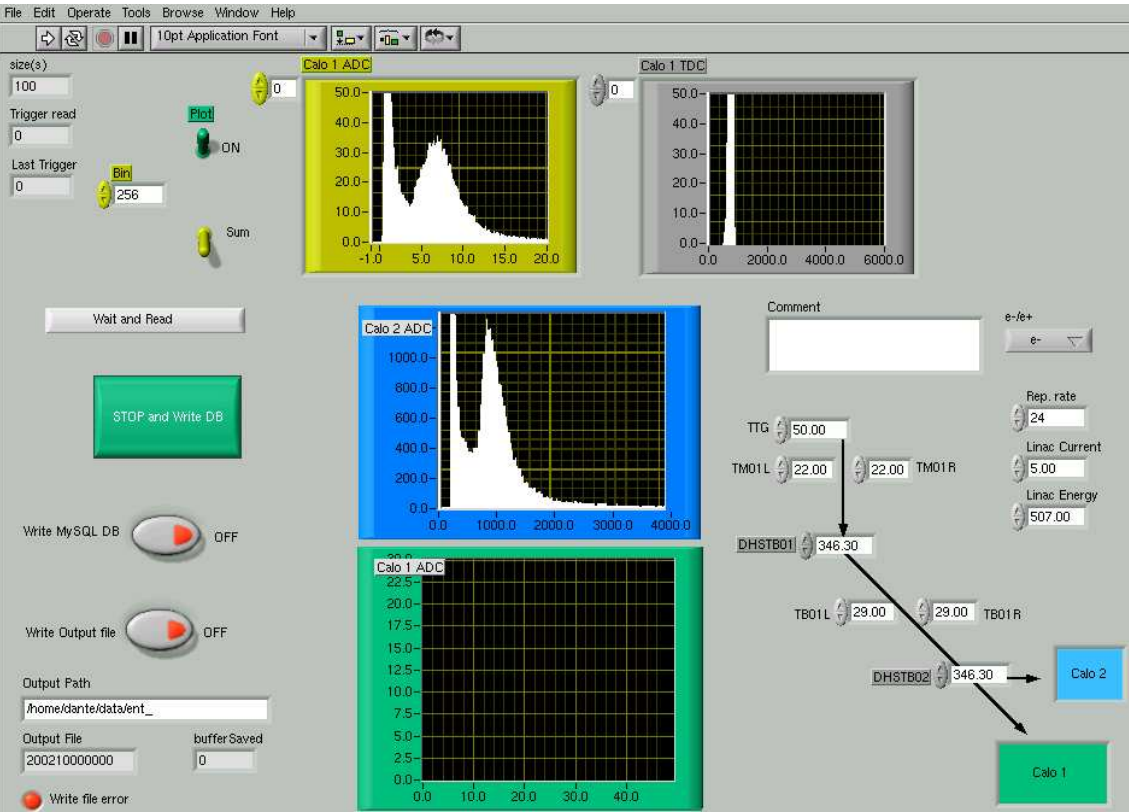

Figure 16: Panel of the LabVIEW program for the run-control, monitoring and storage in the MySQL database.

4.2 Single electron measurement

In the main part of data taking at the BTF, the LINAC setting has been optimized to provide a 510 MeV energy, 4÷5 mA intensity beam, mainly to perform studies in the single particle range. The repetition rate of the LINAC was 24+1 Hz, and the pulse duration was the same as for injection in the accumulator, $\approx$ 10 ns. The typical collimator settings used were 2 mm of total aperture, both for the upstream and downstream slits. In this configuration only a few electrons reach the diagnostic detectors.

Due to the good energy resolution of the calorimeters, $\approx$ 7% at 500 MeV, the number of produced electrons can be counted simply by measuring the total deposited energy E: $n = E/E_1$, where E_1 is the energy deposited by a single electron. The total energy deposited by n electrons will then have a relative error given by:

$$\frac{\sigma_E}{E} = \frac{1}{\sqrt{n}} \frac{\sigma_{E_1}}{E_1} \tag{5}$$

neglecting the intrinsic spread of the beam energy with respect to the detector resolution. The *absolute* width on the nth Gaussian peak should then be:

$$\sigma_n = \sqrt{n} \frac{\sigma_{E_1}}{E_1} \tag{6}$$

In the left plot of Fig. 17 an example of ADC spectrum for the Calorimeter 2 (pedestal subtracted) is shown, for a selected energy of $E_{\text{sel}} = 471$ MeV: the individual peaks corresponding to $0, 1, \ldots, n$ electrons can be easily identified.
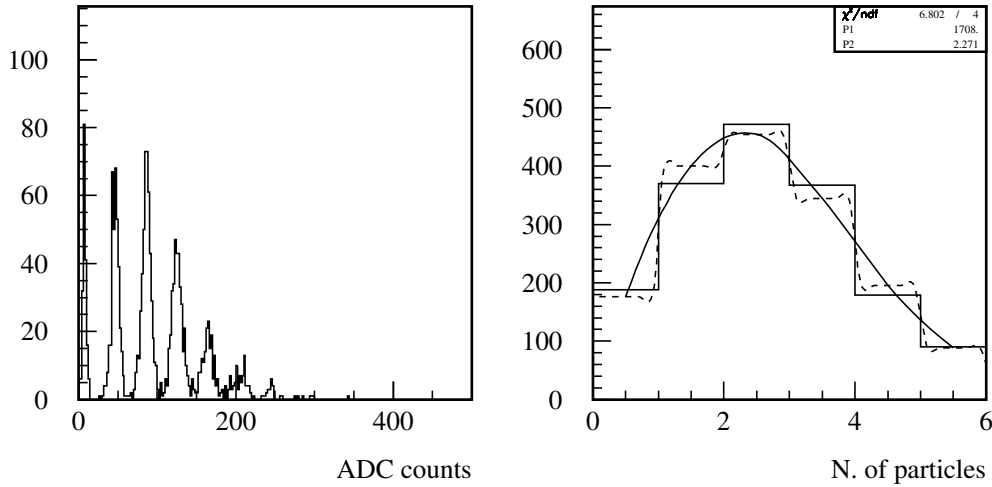

Figure 17: Counting electrons in Calorimeter 2 ($E_{\text{sel}} = 471$ MeV, HV = 1 kV): charge spectrum (left), and Poisson fit of the average number of particles in each peak (right).

The total number of events in each peak should represent the probability of producing n particles. If the average number $\overline{n}$ of produced particles is small, as in this case, those probabilities should be distributed according to the Poisson statistics:

$$P(\overline{n}; n) = \frac{\overline{n}^n}{n!} e^{-\overline{n}}.$$

In the right plot of the same Fig. 17, the distribution of the number of events in each peak is shown, with a fit to the Poisson function, yielding an average number of particles $\overline{n} = 2.3$.

There is an intrinsic limitation to this particle counting method: since the absolute width of the peaks increases with n, as given by Eq. (6), increasing the average multiplicity the peaked structure in the energy distribution gradually disappears, approching a Gaussian shape. The number of particles in the beam can thus be estimated *event by event* only as long as the peaks are clearly separated, *e.g.* at 3σ: the minimum of the nth Gaussian overlaps with the maximum of the $(n-1)^{\text{th}}$ when

$$(n - 3\sigma_n)E_1 \simeq (n-1)E_1$$

corresponding to:

$$n \simeq \frac{1}{9 \left(\sigma_{E_1}/E_1 \right)^2}$$

that in our case gives a limit of $n \approx 20$.

However, the *average* multiplicity $\overline{n}$ can still be statistically estimated from the average of the Gaussian total deposited energy distribution: $\overline{n} = \overline{E}/E_1$.

In this case the fluctuations of the number of particles in the beam, $\sigma_n^2 = \overline{n}$ give the dominant contribution to the relative width of the measured energy distribution,

$$\frac{\sigma_{\overline{E}}}{\overline{E}} = \frac{\sqrt{\overline{n}}}{n}$$

neglecting the primary LINAC beam intensity fluctuations, that can be roughly extimated to be $\delta_{\text{LINAC}} \approx 15\%$ [2]. Thus this approximation gets inaccurate for high multiplicity values, since the approximately constant contribution δ_{LINAC} becomes no longer negligible with respect to the pure Poisson statistics term:

$$\sigma_n/n = \sqrt{1/\overline{n} + \delta_{\text{LINAC}}^2}.$$

An example of an high multiplicity spectrum of E/E_1 is given in Fig. 18: the peaks corresponding to the discrete values of n are no longer resolved, but the average number of particles can be estimated by a Gaussian fit, $\overline{n} \simeq 40$.
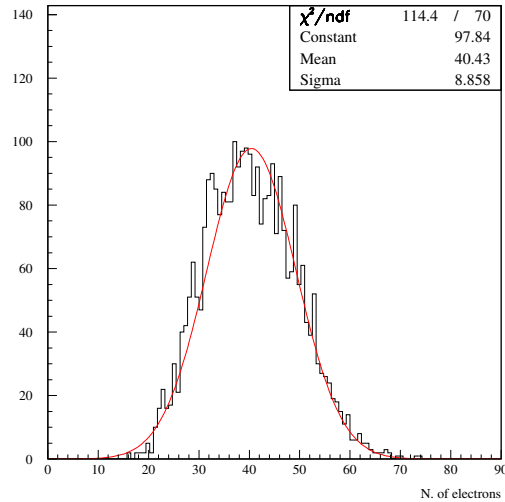
Figure 18: Signal in Calorimeter 2 with respect to the single electron average deposited energy, corresponding to the number of delivered particles: $n = E/E_1$.

Another intrinsic limitation to the particle counting performed by means of the total energy measurement in a calorimeter is the detector saturation, *i.e.* when the signal begins to be no longer proportional to the number of particles. This is in general due to one or more of the following factors: saturation of the ADC scale, of the photomultiplier gain or the scintillation light yield. In our case the main problem is the saturation of the photomultiplier gain.

Thanks to the excellent performances of the lead/scintillating fibers calorimeter, the time distribution of the energy depositions should reflect the time structure of the LINAC pulse; in particular a flat distribution, 10 ns wide, should be observed. The timing resolution of the fibers at these energies, on the other hand, is not good enough to resolve the 300 ps microbunch structure. The time distribution for the same events of Fig. 17 is shown in the right plot of Fig. 19, together with the correlation with the measured pulse height. Even though a slewing effect is clearly visible, the width of the distribution is essentially the expected 10 ns for the first peaks; then the width gets smaller when more than one electron is detected, since the used TDC is a single-hit one and can only measure the time of the fastest signal.

The same results can be obtained using Calorimeter 1, once the gains of the 14 cells are equalized. The calibration of each cell is performed by selecting horizontal cosmic rays, traversing the detector. The energy deposited in a cell by a minimum ionizing particle (1 MIP) is used as reference, and the HV settings are adjusted in order to equalize all the channels response. An example of cosmic ray spectrum is shown in Fig. 20, with a fit to
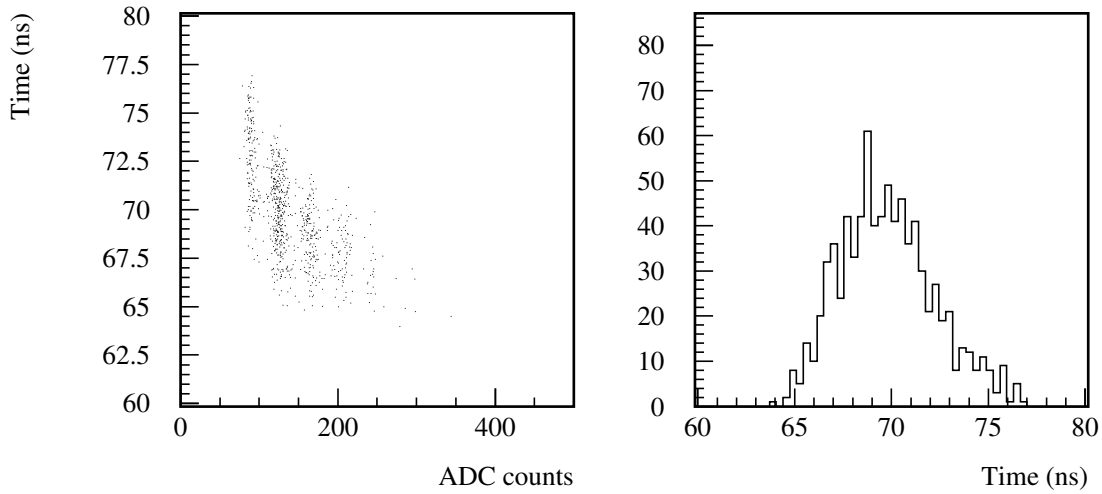
23

Figure 19: Counting electrons in Calorimeter 2 ($E_{\mathrm{sel}} = 471$ MeV, HV = 1 kV): time vs. charge distribution (left) and corresponding time spectrum (right).

the Landau distribution; in the right plots of the figure, an example of the most probable values for the energy deposited by cosmics (in ADC counts) are shown together with the HV settings.
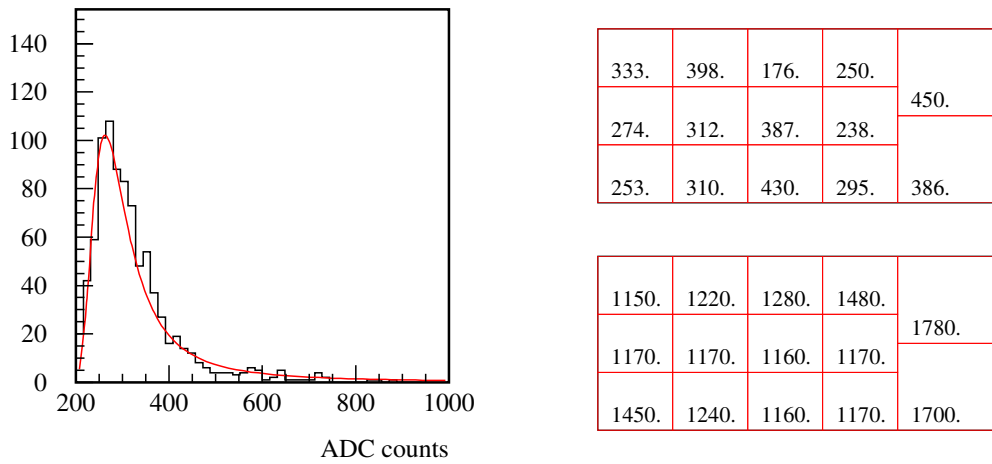

Figure 20: Calorimeter 1: example of 1 channel cosmics spectrum with superimposed Landau fit (left); mip average value (top right) and HV settings (bottom right) for the 14 channels.

Calorimeter 1 has been mainly used to detect low energy electrons; an example of the total energy deposited in Calorimeter 1, after gain equalization and expressed in MIP units, is shown in Fig. 21, for a selected energy of E_{sel}=80 MeV. The peaks of one or two electrons entering the calorimeter are still resolved; they have been fitted with a sum of

two Gaussians.
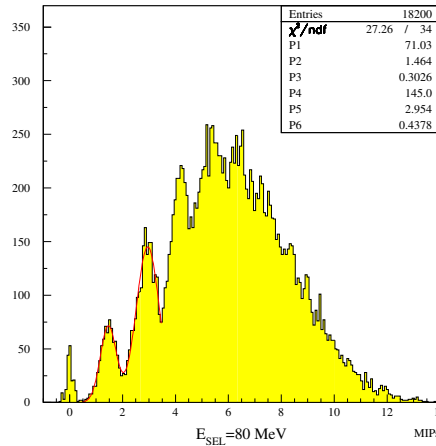
Figure 21: Energy deposited in Calorimeter 1 for E_{sel}=80 MeV after gain equalization, the Gaussian fit to the first and second electron peak is also shown.

The average measured energy should be proportional to the incoming beam energy, while the resolution should scale as $1/\sqrt{E_{sel}}$. This can be experimentally verified by performing the same energy measurement for different E_{sel} values (changing the first dipole current). In Fig. 22 the average value and the width of the single electron peak is shown as a function of E_{sel}. The observed energy is fairly proportional to the beam nominal energy, and the relative width shows a $1/\sqrt{E_{sel}}$ behaviour, as expected. The deviation from the linear shape is due to the fact that the energy selector magnet DHSTB01 did not always perform standard magnetization cycles for each point of the scan.

Even though no beam profile detector was available in 2002, an estimate of the beam spot size can be obtained by measuring the particle multiplicity as a function of the collimator aperture. In Fig. 23 the measured average multiplicity is plotted as a function of the aperture of the SLTTB01 collimator (downstream the bending magnet). The saturation value is consistent with what expected for a beam of a few mm size.

4.3 High multiplicity measurement

The most effective way to change the average number of particles in the beam (as discussed in Sec. 3.1), is to change the selected energy; in particular, at the **same** LINAC energy and intensity and with the **same** collimator settings, the multiplicity increases by lowering the chosen E_{sel}. The energy measured by Calorimeter 2 is shown in Fig. 24 , together with the Poisson fit to the multiplicity distribution, for a selected energy of 442
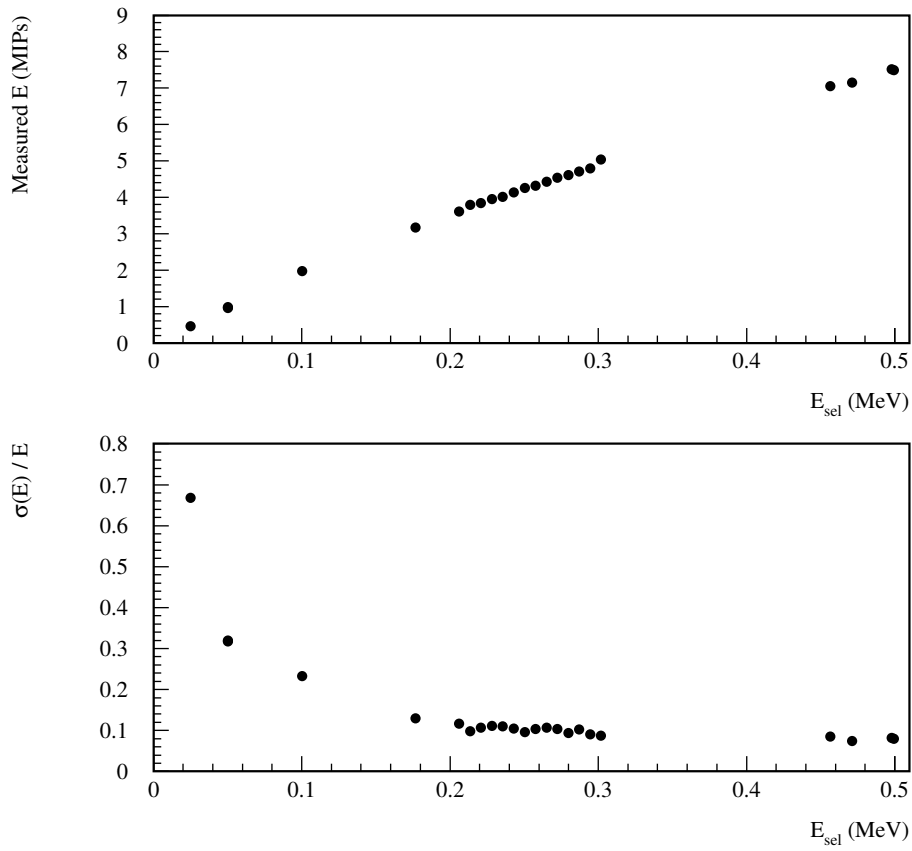
Figure 22: Energy deposited in calorimeter 1: the average (top) and relative width (bottom) of the Gaussian fit to the first electron peak is shown as a function of E_{sel} (calculated on the basis of the bending magnet setting).
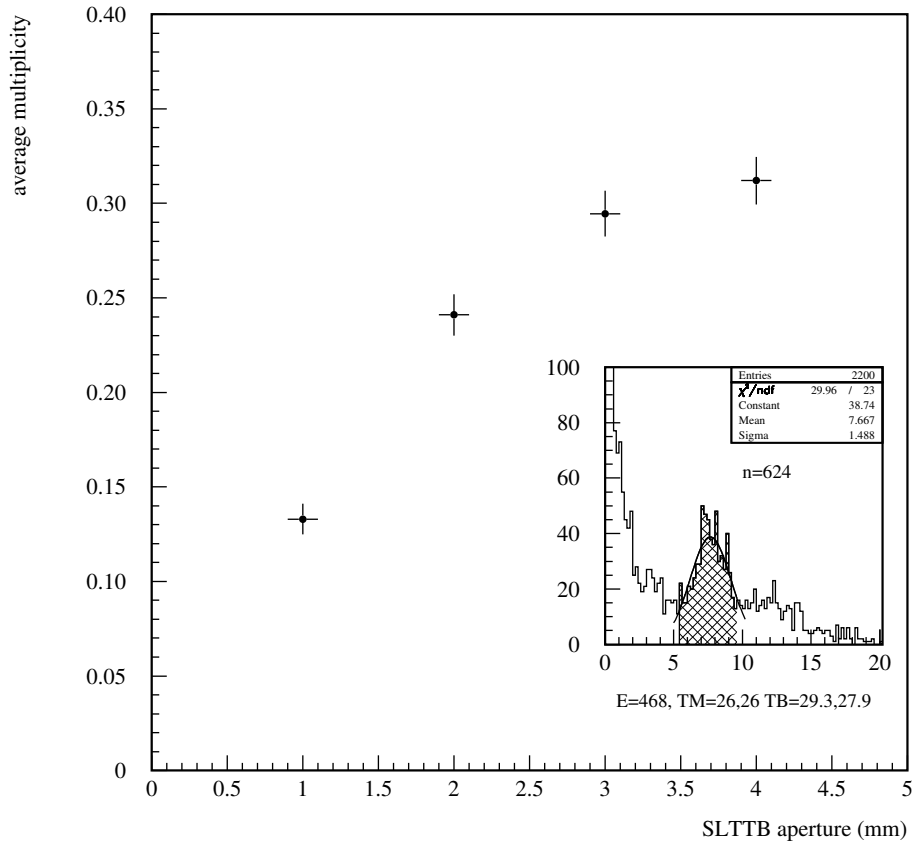
Figure 23: Measured multiplicity as a function of the downstream collimator aperture (SLTTB01).

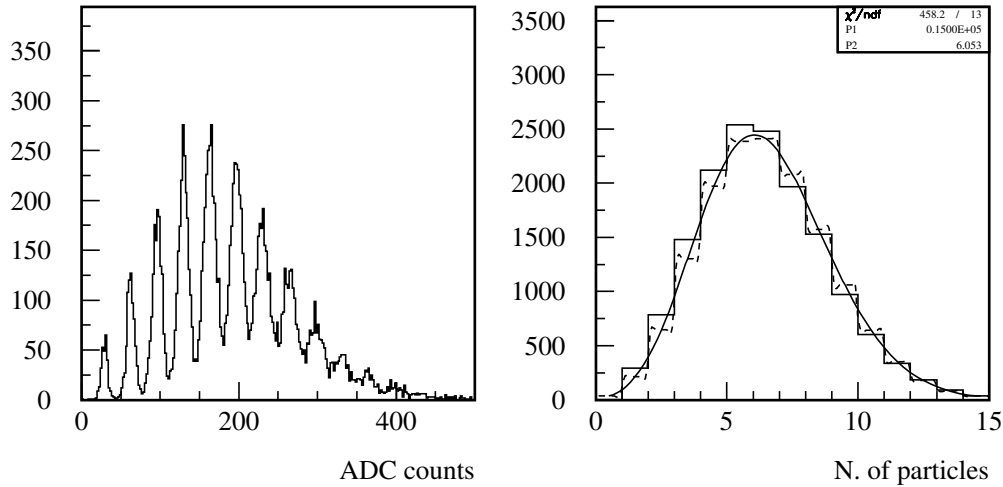MeV: as compared to the spectrum of Fig. 17 at 471 MeV, the average number of particles increases from 2.3 to 6.0.

Figure 24: Counting electrons in Calorimeter 2 ($E_{\text{sel}} = 442$ MeV, HV = 1 kV): charge spectrum (left), and Poisson fit (right).

Calorimeter 2 has been generally operated at a lower gain (with respect to the optimal one for an optimal energy resolution, as for Calorimeter 1) in order to span a wider multiplicity range. The response of the detector, in fact, is still proportional to the number of electrons up to ≈ 10 particles. The average value of the peaks of the ADC spectrum (pedestal subtracted) is shown in Fig. 25, together with a linear fit, showing essentially no saturation.

By lowering more and more the selected energy, in the same conditions, the multiplicity keeps increasing. In the limit in which the number of particles can still be measured with a resonable resolution (as discussed in Sec. 4.2), the number of produced particles as a function of the selected energy can be compared with what expected from the Monte Carlo simulation described in Sec. 3.2. In Fig. 26, the Monte Carlo and experimental distributions of the average number of particles $\overline{n}$ as a function of E_{sel} is shown: the shapes are pretty similar, even though the data points are lower due to the transport inefficiencies and the further reduction introduced by the collimators.

The multiplicity can thus be tuned not only by varying the selected energy, but also by changing the aperture of the upstream and/or downstream collimators. In this case the energy resolution of the selector will be also affected, but by a relatively small amount, as discussed in Sec. 3.1, in any case well below the intrinsic resolution of our calorimeters. The measured multiplicity should then increase by increasing the slits aperture; this is
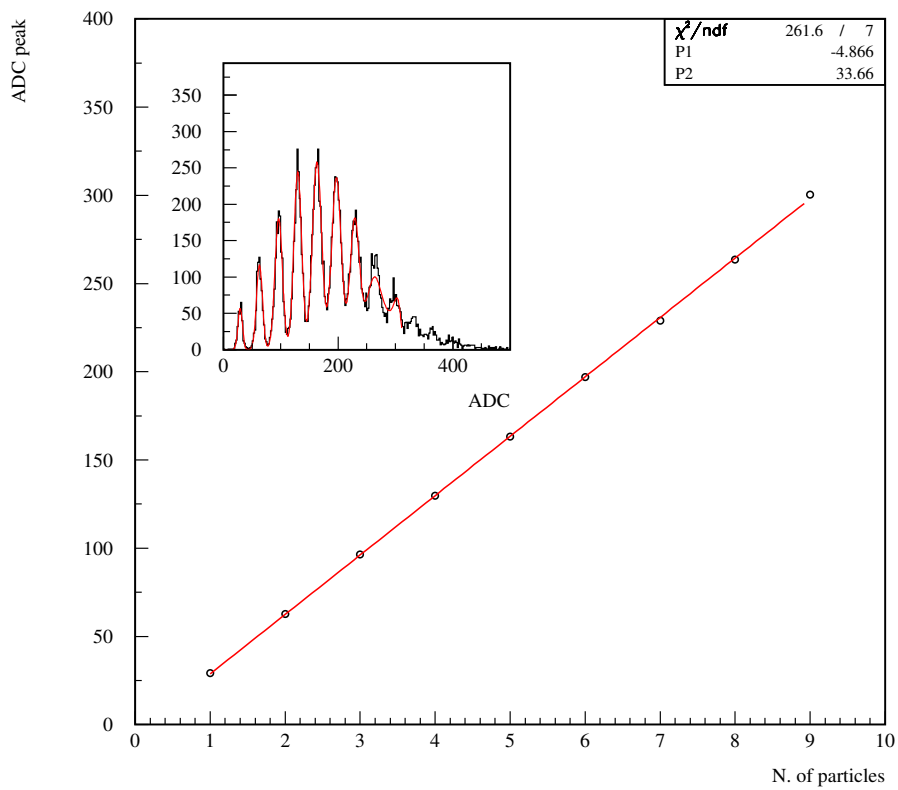
28

Figure 25: Counting electrons in Calorimeter 2 (E_{sel} = 442 MeV, HV = 1 kV): peaks linearity (in the inset: multi-Gaussian fit to the ADC spectrum).
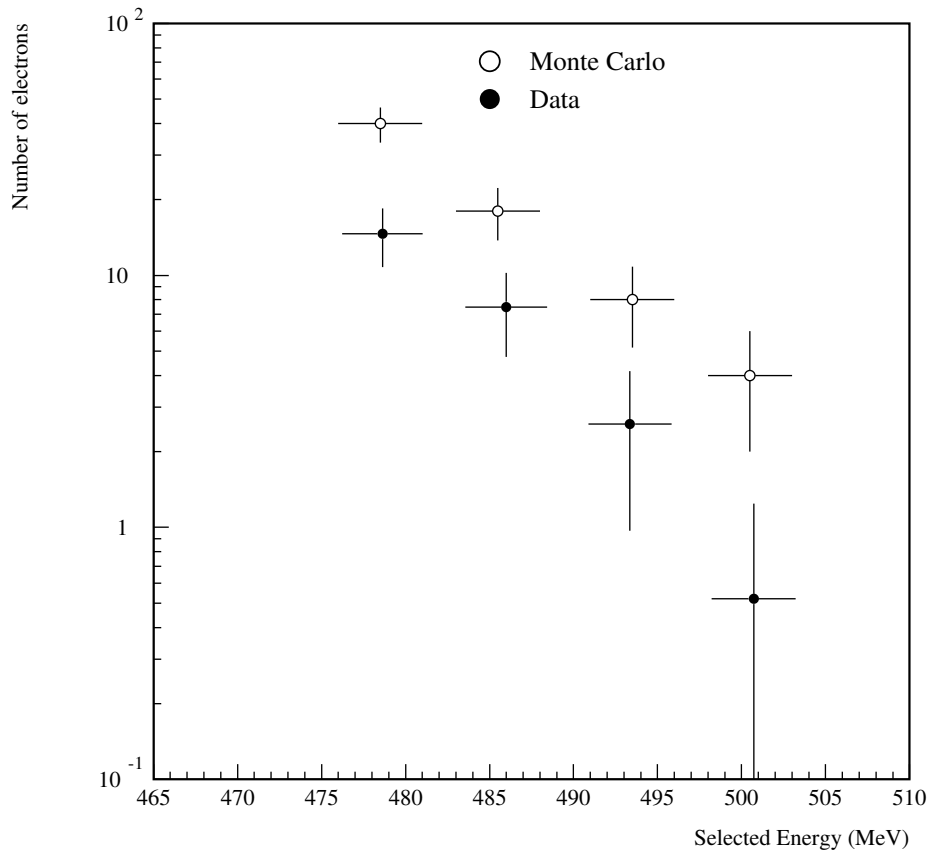
Figure 26: The expected number of particles as a function of the selected energy (with a 1% acceptance) estimated from the Monte Carlo (empty dots) are compared with the measured multiplicity (full dots).

true until the intrinsic beam spot size (*at the downstream slit*) is exceeded (as discussed in Sec. 4.2).

Another way of varying the average number of particles at the BTF exit is to change the LINAC current. The LINAC beam intensity can be changed by modifying a number of different parameters, such as the modulators power and phases, the LINAC gun current, or the beam focussing. This reflects into different beam characteristics at the degrader target. Anyhow, the measured multiplicity increases by increasing the LINAC beam intensity, as shown in Fig. 27.
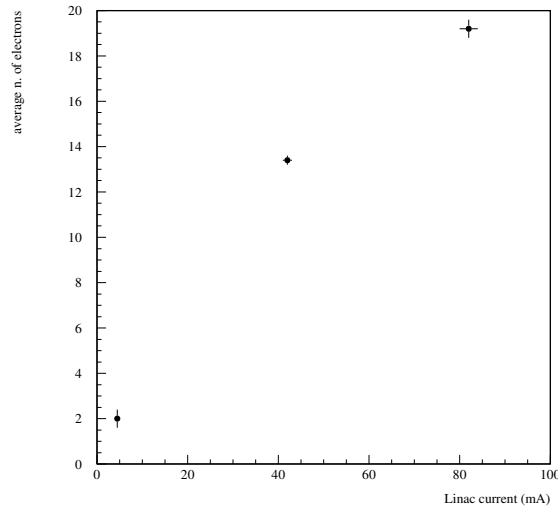
Figure 27: Measured multiplicity as a function of the LINAC current.

4.4 Diagnostic detectors: Cerenkov counter

Going further up in the number of produced particles the calorimeters are no longer effective mainly due to saturation effects (see Sec. 4.2). In order to have a diagnostic device in the $\overline{n} = 100\text{-}1000$ range (and higher), a different detector has been developed and tested in collaboration with the AIRFLY group [13].

It is essentially a counter based on the Cerenkov light emission in a PLEXIGLAS radiator when transversed by relativistic electrons (which in the BTF energy range is always the case). The radiator has a circular section and is shaped as a bent cylinder in order to transport away from the beam line direction the Cerenkov light – emitted at an angle θ_C – by total internal reflection. The light is then extracted thanks to the appropriate shaping of the end part of the radiator itself: a conical shape with the proper opening angle $(90° - \theta_C)$ is carved into the bent cylinder. Finally, the light is collected by a

31

photomultiplier tube, without optical connection: this gives the possilibity of interposing a calibrated optical filter (fused silica neutral density filter) between the radiator and the PMT, in order to attenuate the Cerenkov light by a known factor; this eventually allows to extend the dynamical range of the counter. The diameter of the bent cylinder is 2 cm; the detector is schematically shown in Fig. 28.
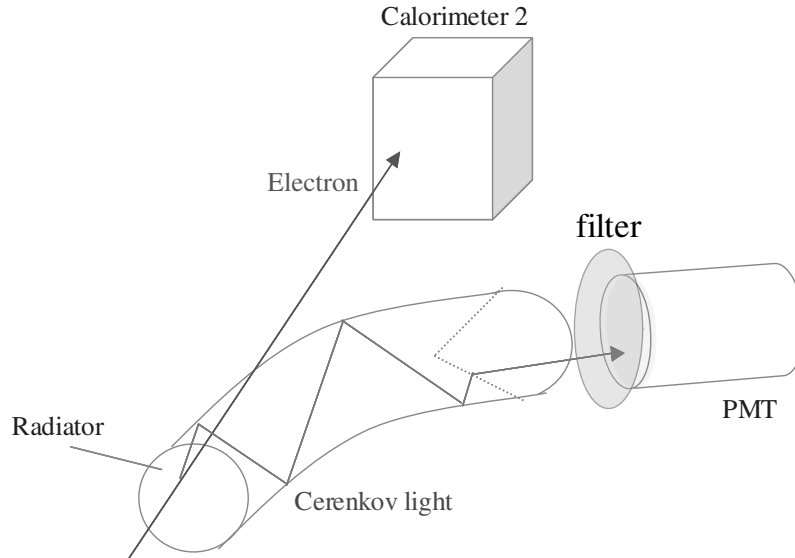

Figure 28: A small Cerenkov counter (from the AIRFLY experiment) was used to measure the number of electrons at high multiplicity; the plexiglas radiator of bent cylindrical shape has a diameter of 2 cm.

The analog signal from the photomultiplier, properly delayed, is fed to the same DAQ chain as the ones of the two calorimeters and integrated with the same 250 ns gate signal (see Sec. 4.1). The discriminator threshold is set to a suitably lower value of 8 mV/50Ω, in order to be sensitive to the single electron.

The Cerenkov light yield, and in turn the phototube analog signal, should be proportional to the number of electrons traversing the radiator; this phenomenon should be linear up to a very high number of electrons. The charge spectrum of the Cerenkov detector signal, compared with the energy in the calorimeter, is shown Fig. 29 (in the few particles range). The signal in the Cerenkov counter for one or few delivered electrons does not show resolved peaks. This is not only due to the worse intrinsic resolution, but it is mainly related to the very small signal, close to the pedestal, and to pedestal width itself since the gate width was tuned for the calorimeters. Moreover the beam spot size, $\sigma \approx 5$ mm (see in the following and Sec. 4.2), is comparable with the diameter of the radiator (20 mm), thus spoiling the single electron resolution.
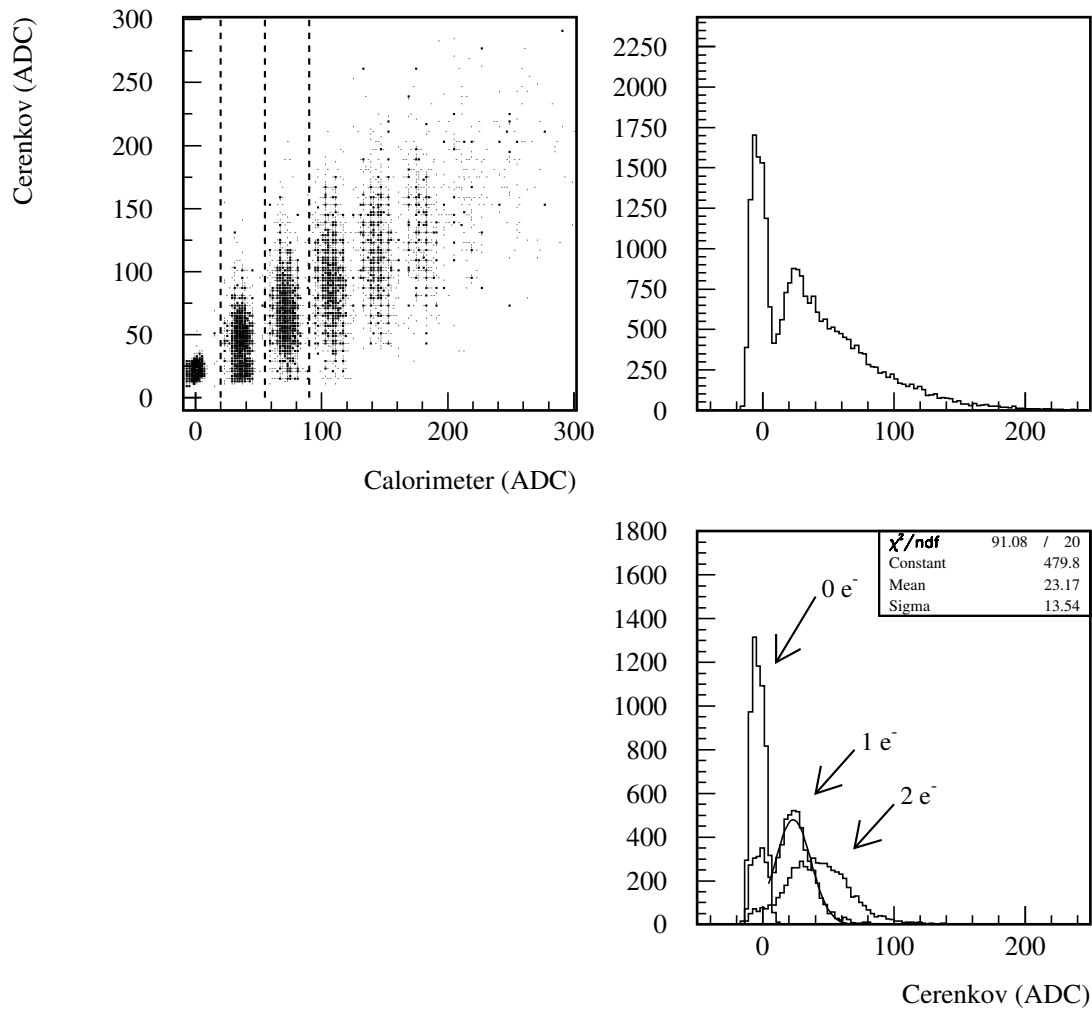
Figure 29: Left top: signal in the Cerenkov counter vs. signal in the calorimeter (ADC counts). Right: the Cerenkov signal spectrum without cuts (top) and for 0,1,2 electrons in the calorimeter (bottom).

The comparison between the two signals has been performed also in the high multiplicity region (≈ 40, for the same data of Fig. 18, $E_{\text{sel}} = 471$ MeV), and is shown in Fig. 30. There is a strong correlation between the two signals, the slope has been estimated from the average of the distribution of the ratio between the two ADC values (pedestal subtracted).
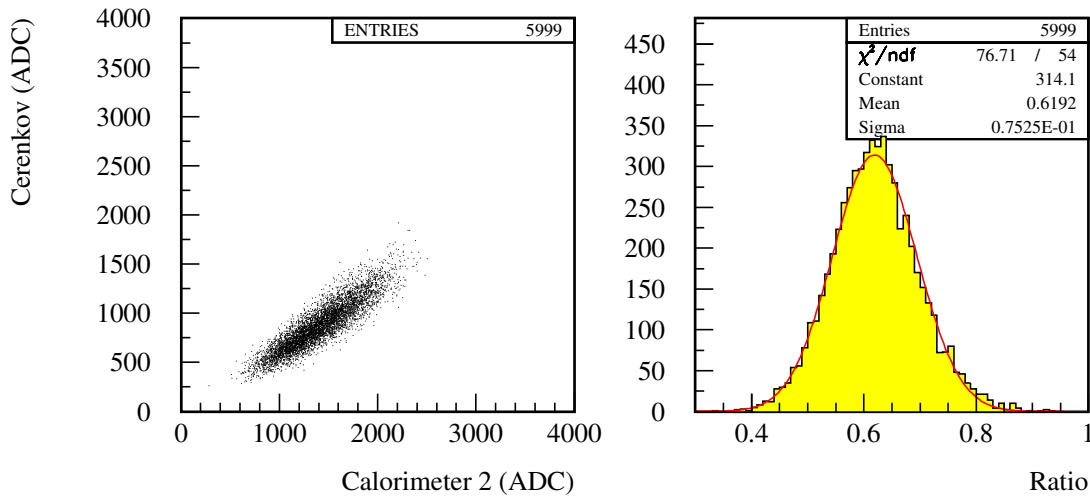
Figure 30: Signal in the Cerenkov counter vs. signal in the calorimeter, in ADC counts (left), ratio of the two signals with Gaussian fit (right) for $E_{\text{sel}} = 471$ MeV.

The same measurement has been repeated in the same conditions, but interposing a calibrated optical filter – with attenuation factor 10 – between the radiator and the photomultiplier. The correlation between the Cerenkov and Calorimeter 2 signals is shown in Fig. 31, together with their ratio: the measured attenuation factor is 10.4 ± 0.3. Using this cross-calibration, the Cerenkov counter has been used to monitor the beam multiplicity up to ≈ 1000, as shown in Fig. 32.

The Cerenkov counter and calorimeter signals have been also used to measure the horizontal acceptance of the beam line with the method described in the following. As described in Sec. 2.1, the last dipole magnet, DHSTB02, allows to select either the straight exit, at zero current, or the 45° angle exit, when set to the same current of DHSTB01 selector magnet (for particles travelling at the beam-pipe center). The horizontal bending angle of the beam can thus be changed by varying the current setting of the last dipole. The observed yield in the detector should be constant as a function of the bending angle, until the beam exits the angular acceptance (in the horizontal plane) of the detector or it hits the beam pipe wall.

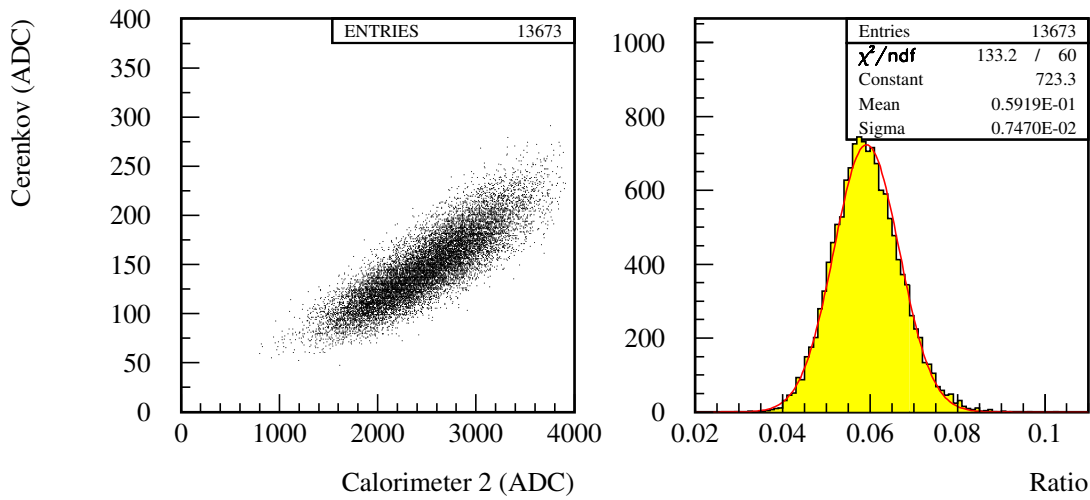This can be clearly seen in Fig. 33 where the measured multiplicity in Calorimeter 2 and

Figure 31: Signal in the Cerenkov counter vs. signal in the calorimeter, in ADC counts (left), ratio of the two signals with Gaussian fit (right) when an optical calibrated filter (nominal attenuation factor = 10) is inserted between the radiator and the photomultiplier ($E_{\text{sel}} = 471$ MeV).
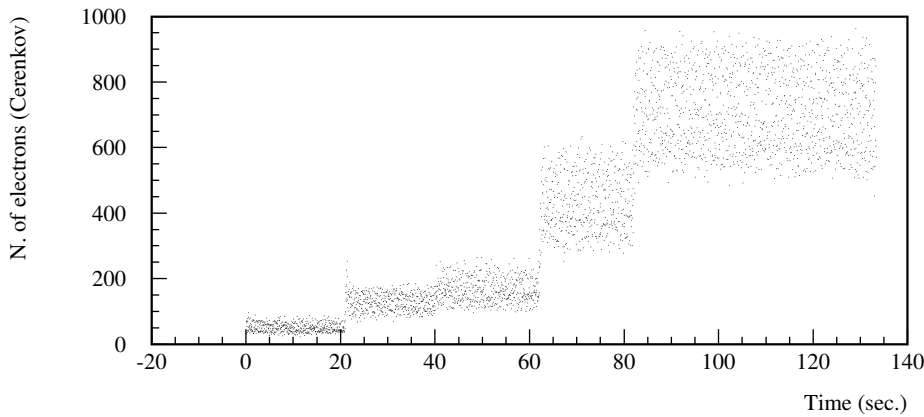

Figure 32: Number of estimated particles in the Cerenkov counter (after normalization with Calorimeter 2 yield) as a function of time: the average multiplicity during the run has been increased by opening the collimators.

in the Cerenkov counter are shown as function of the bending angle. While the yield in the Cerenkov reflects the shape of the PLEXIGLAS radiator and drops to zero when the beam exceeds the detector acceptance, the signal in the calorimeter is constant until the beam reaches the beam pipe diameter. The distribution has been fit with a Fermi-like function (Gaussian edged box) to evaluate the half-width and the Gaussian smearing at the edges. Taking into account the calorimeter/magnet distance, $L = 1380$ mm, the half-width of the distribution is compatible with the nominal pipe radius, $r = 30$ mm: $(24 \pm 2) \cdot 10^{-3} \times 1380 = 33 \pm 3$ mm. The angular width of the Gaussian edge, *i.e.* when the beam hits the pipe wall, gives instead an indication of the beam spot size *at the line output*: $\sigma_x = (3.7 \pm 0.3) \cdot 10^{-3} \times 1380 = 5.0 \pm 0.4$ mm.
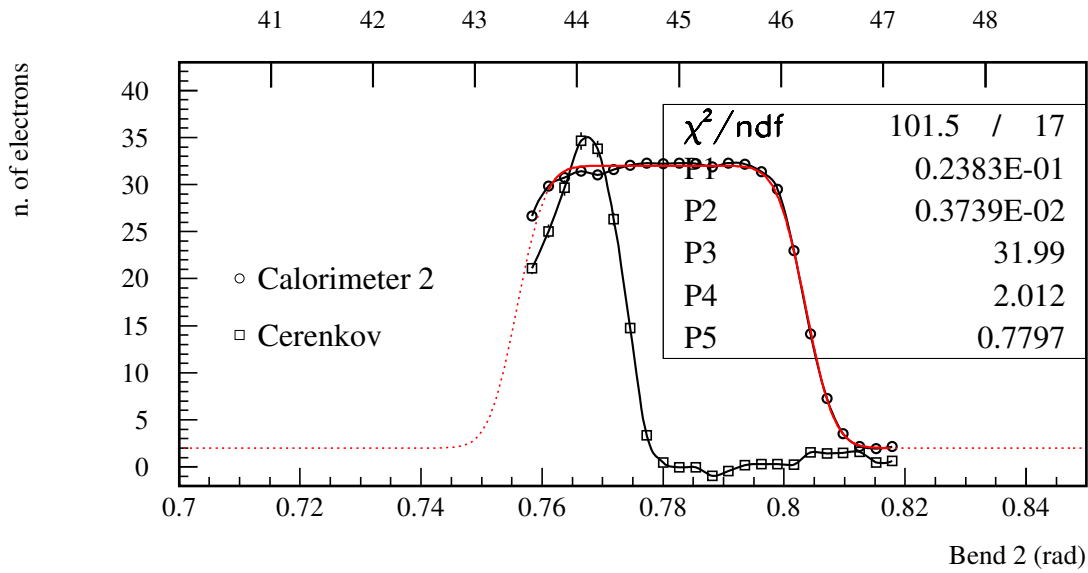

Figure 33: Average number of electrons in the Cerenkov counter and in Calorimeter 2 as a function of the second dipole current, translated in bending angle in radians (bottom scale) and degrees (top scale), for $E_{\text{sel}} = 471$ MeV.

5 Operational experience

5.1 Dedicated and parasitic operation

After a first period in Febrary 2002, the measurement of the beam characteristics (described in previous sections) and the first users data taking took place from Oct. 29 to Dec. 20, 2002. During this phase the DEAR experiment was running at the second interaction point of the DAΦNE main rings. This allowed to use the LINAC for BTF operation only between two injection cycles, so that we call "parasitic mode" this mode of operation. Another possibility is the "dedicated mode", when the BTF runs with no collisions at all in the main rings, and the facility can be used 24h/day; however this is restricted to the maintenance/shutdown periods of the main experiments at the collider.

The typical bunch configuration in 2002 DEAR runs was $100 + 100$ bunches; an injection cycle during the DEAR runs is the following:

1. electrons are injected into the accumulator and from there into the e^- main ring at 1 Hz repetition rate; it requires 2-4 min. (100 bunches $\times$ 1 sec. $\times$ n. of fillings);

2. the LINAC and transfer lines are switched to positron mode; typically 3.5 min. are needed (essentially due to the magnets ramping);

3. positrons are injected in accumulator/e^+ ring at 1 Hz; 2-4 min. are required;

4. DEAR run starts, switch to BTF mode: the target and collimator slits are inserted, magnets are cycled and ramped on (1-2 min.);

5. BTF beam can be delivered until 3.5 min. before next DEAR injection; typically 20-25 min.

A complete cycle in this configuration lasts 40-45 min. The time chart of e^+/e^- currents in the two main rings are shown in Fig. 34 during a couple of injection cycles during the DEAR data taking, the phases enumerated above are also indicated. This corresponds to a duty-cycle for the BTF operation of about 50%.

During the KLOE experiment operation, data taking does not stop during injections, so that DAΦNE is operated in "topping up" mode: the injection cycles lasts only 15-20 min. to optimize the average luminosity. This leaves essentially no time for the BTF "parasitic mode".

The other feature of the "parasitic mode" was that the LINAC energy could not be easily changed (mainly for practical reasons).
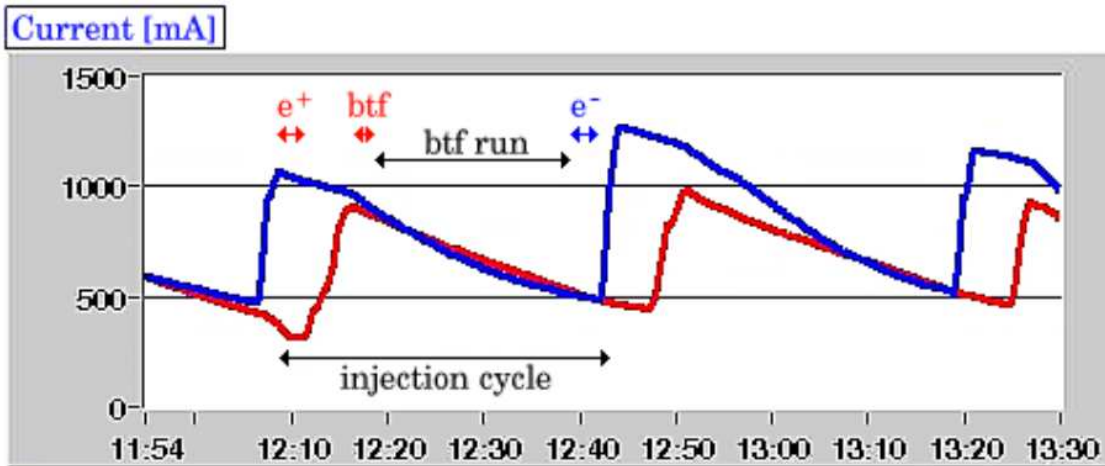
Figure 34: Time chart of the electron and positron currents in the main rings showing a typical 'parasitic' BTF run: after electron injection in the main ring the LINAC is switched to positron injection (3.5 min. for the switch); once e$^+$ injection is completed the LINAC is switched to BTF (in 1.5 min.). The BTF run can last up to the next electron injection (3.5 min. again needed to switch to e$^-$). During DEAR operation electron injections occured every $\approx$ 40 min., so that the BTF duty cycle was about 50%.

5.2 First users access

Two user tests were carried on in the Nov.-Dec. 2002 period: the AIRFLY experiment (air fluorescence yield measurement) [13], and the LCCAL [14] electromagnetic calorimeter test. This two first users represented two extreme operation mode of the BTF facility:

> **AIRFLY**: high multiplicity in a wide range of energies (the widest accessible for the BTF beam), detector in a fixed position;
>
> **LCCAL**: single electron for a few energy points, full coverage of the detector by moving it across the beam;

This was also nicely fitting the measurement campaign for the beam characterization in the several possible configurations.

The BTF demonstrated to be easily tuneable both from the point of view of the desired particle multiplicity (from single electron mode to $\approx$ 1000, see Sec.4.4) and energy setting (see Fig. 22).

Moreover, the "parasitic operation" mode has been successfully tested.

6 Conclusions and future perspectives

The commissioning results, as well as the first user experience, have demonstrated that the DAΦNE Beam Test Facility can be operated with very high reliability. It has also shown a very high versatility in producing different configurations, both in energy and multiplicity, with a good stability.

In order to overcome the present limitations imposed by KLOE operation, where practically no time is now left for beam delivery in the BTF test area, but also to largely improve the duty-cycle during FINUDA operation, we plan to upgrade the facility in January 2004 during the DAΦNE cryogenic system maintenance [15].

A complete separation between the DAΦNE transfer lines to the Main Rings and the BTF channel will allow to operate in the BTF mode with the only limitations of the LINAC switching time and the time spent for filling the Main Rings. A duty-cycle of order of 80% during KLOE, and around 90% in FINUDA operation, is expected.

More diagnostic systems, especially devoted to beam profiling, as well as high multiplicity measurement, are under development in order to improve the characterization of the beam quality.

References

[1] The DAΦNE Project Team, *Proposal for a φ-factory*, LNF-90/031 1990;
S. Guiducci *et al.*, *Status report on DAΦNE*, in Proceedings of PAC 2001, Chicago, USA (2002).

[2] F. Sannibale, G. Vignola, DAΦNE Techical Note **LC-2** (1991), unpublished[1]
A. Ghigo, F. Sannibale, *Single Electron Operation Mode in DAFNE BTF*, in Proceedings of EPAC 94, London (1994) 2444.

[3] G. Di Pirro *et al.*, *The Evolution of the DAΦNE control system: A History of liberation from hardware*, in Proceedings of ICALEPCS 2001, San Jose, USA (2002).

[4] O. Coiro, G. Galletti, DAΦNE Techical Note **CD-11** (2001), unpublished[1].

[5] F. Sannibale, M. Vescovi, *LINAC to Accumulator Area Transferline and DAFNE-LINAC Spectrometer*, DAΦNE Techical Note **LC-3** (1992), unpublished[1].

[6] A. Battisti *et al.*, *Measurement and tuning of DAΦNE accumulator dipoles*, DAΦNE Techical Note **MM-9** (1995), unpublished[1];
M. Preger, private communication.

[7] B. Rossi, *High Energy Particles*, Prentice-Hall, Inc., N.Y., USA (1952).

[8] GEANT 3.21, CERN Program Library, Long Writeup **W5013**.

[9] D.C. Carey *et al.*, SLAC-R-530 (1998).

[10] A. Aloiso *et al.*, Nucl. Instrum. Meth. A **482** (2002) 363.

[11] A. Antonelli *et al.*, Nucl. Instrum. Meth. A **354** (1995) 352.

[12] G. Mazzitelli *et al.*, Nucl. Instrum. Meth. A **486** (2002) 568.

[13] P. Privitera *et al.*, *AIRFLY Letter of Intent*, INFN Gr. V, unpublished.

[14] S. Bertolucci *et al.*, *Construction and test of an Electromagnetic calorimeter prototype*, DESY PRC R&D 00/02.

[15] G. Mazzitelli *et al.*, *DAFNE Beam Test Facility Upgrade Proposal*, DAΦNE Techical Note **BTF-1** (2003), unpublished[1].

---

[1]DAΦNE notes are available at **http://www.lnf.infn.it/acceleratori/**